Energy 354 (2026) 140984

Contents lists available at ScienceDirect

Energy

journal homepage: www.elsevier.com/locate/energy

High-power-density energy harvester via optimized negative Poisson's ratio metastructure with nonlinear gradient wall thickness

Shitong Fang [a,b], Jinkang Liu [a,b], Yufeng Guo [a,b], Qingyang Xu [c], Kui Wu [a,b], Yi Guan [a,b], Liuchao Jin [e], Zhihui Lai [a,b], Mingjing Cai [d], Keyu Chen [e,*], Wei-Hsin Liao [e,*]

[a] Guangdong Key Laboratory of Electromagnetic Control and Intelligent Robots, College of Mechatronics and Control Engineering, Shenzhen University, Shenzhen, 518051, China
[b] National Key Laboratory of Green and Long-Life Road Engineering in Extreme Environment (Shenzhen), Shenzhen University, Shenzhen, 518051, China
[c] School of Mechatronic Engineering and Automation, Shanghai University, Shanghai, 200444, China
[d] Guangzhou Institute of Technology and School of Mechano-Electronic Engineering, Xidian University, Guangzhou, 510555, China
[e] Department of Mechanical and Automation Engineering, The Chinese University of Hong Kong, Shatin, Hong Kong, 999077, China

ARTICLE INFO

Keywords:
Piezoelectric energy harvester
Negative Poisson's ratio structure
Nonlinear gradient supercell wall thickness
Multi-objective optimization
Self-powered wireless sensing

ABSTRACT

With the advancement of the Internet of Things (IoT), miniature low-power electronic devices have become prevalent in vibration-detection applications. However, miniaturized cantilever piezoelectric energy harvesters often exhibit insufficient power at low frequencies. To address this limitation, this study proposes a negative Poisson's ratio energy harvester with nonlinear gradient supercell wall thickness (NEH). The proposed harvester is compared with a plain energy harvester (PEH) and a negative Poisson's ratio energy harvester with uniform wall thickness (UEH) using parametric 3D modeling, finite element analysis, and experimental evaluations. The findings indicate that the NEH has a lower fundamental resonant frequency, as well as more uniform stress–strain distribution that leads to higher output voltage and power. Subsequently, multi-objective optimization aimed at maximizing power and minimizing stress is conducted using an optimal Latin hypercube design, neural network, and non-dominated sorting genetic algorithm II. This process results in an optimized energy harvester (OEH), which reduces the maximum stress by 11.85% compared with NEH and achieves a power density of 124.89 μW/g, representing increases of 94.1%, 186.8%, and 348.56% compared with NEH, UEH, and PEH, respectively. The OEH achieves a normalized power density of 374.11 μW cm^{-3} Hz^{-1} that surpasses the previous works. Finally, a vibration-driven wireless sensing system (VPSS) is constructed to validate the performance of the proposed energy harvesters, enabling data transmission over approximately 200 m. Under an excitation of 5 m/s^2, the OEH facilitates temperature signal transmission with 37.5% higher efficiency compared to the NEH, demonstrating significant potential for self-powered wireless monitoring of vibrating equipment.

1. Introduction

The global pursuit of energy-efficient and sustainable solutions, driven by energy scarcity and environmental concerns, has positioned energy-harvesting technology as a pivotal field [1–3]. This technology captures ambient energy from sources like light, heat, and vibration for conversion into electricity. Among these, vibration energy harvesting holds significant potential for powering wireless sensors to monitor industrial and natural systems, given the ubiquity of environmental vibrations [4,5]. Piezoelectric conversion has become the most prevalent of the three primary mechanisms (electrostatic [6], electromagnetic [7–11], and piezoelectric [12–16]), owing to its high power density, ease of miniaturization, and environmental robustness. These advantages have led to its widespread adoption in diverse applications, from industrial condition monitoring and wind energy capture to biomedical devices like pacemakers and wearable technology [8].

Piezoelectric energy harvesters employing cantilever beam architecture, comprising a piezoelectric layer bonded to a clamped end and a proof mass at the free end, have attracted significant research attention due to their structural simplicity and operational efficacy. Nevertheless, as inertial linear resonators, their output power is maximized only near the resonant frequency. Besides, with the harvester volume reduced, its resonant frequency will be increased, leading to the low power output at low frequencies. In practical environments, vibration

* Corresponding authors.
E-mail addresses: kychen@link.cuhk.edu.hk (K. Chen), whliao@cuhk.edu.hk (W.-H. Liao).

https://doi.org/10.1016/j.energy.2026.140984
Received 20 February 2026; Received in revised form 27 March 2026; Accepted 6 April 2026
Available online 17 April 2026

frequencies frequently fluctuate with operational conditions, such as varying machine loads, and even minor deviations in frequency can lead to a significant decline in performance, thereby failing to satisfy the power requirements of microelectronic devices. Furthermore, the ambient vibrations are normally distributed within a low-frequency range. Consequently, enhancing the energy-harvesting efficiency of cantilever beam designs at low vibration frequencies remains a critical objective.

To address the above limitation, researchers have investigated structural optimization, material innovation, circuit design, and the application of multi-stable systems. In particular, structural optimization has led to significant advances in this field. Nabavi and Zhang [17] developed a MEMS-based T-shaped harvester that distributed mechanical strain over a wider area, achieving a power density 4.8 times that of traditional cantilevers. Yang et al. [18] incorporated an arc-shaped structure, whose low stiffness enables large, uniform stress distribution, resulting in 4.25 times higher output power than flat designs under identical conditions. Ibrahim et al. [19] designed a gauge-shaped beam with a lower resonance frequency and higher output power, suitable for low-frequency ambient vibrations. Leveraging the larger piezoelectric coefficient d_{15} (compared with d_{31} for most materials), Malakooti and Sodano [20] developed a shear-mode harvester that generated 50% more power than the transverse-mode (d_{31}) designs under the same excitation. Xu et al. [21] combined a cymbal transducer with a cantilever, using the cymbal's force amplification and the cantilever's flexibility to achieve high power under low-frequency excitation. Yang et al. [22] designed a compression-mode harvester with a two-stage force amplification mechanism, producing 19 mW under low-frequency weak excitation (4.9 m/s^2 at 21 Hz), ideal for low-intensity environments.

In recent years, the use of negative Poisson's ratio (NPR) metastructure in piezoelectric harvesting has increased to boost the output while reducing the mass and volume, thereby improving the power density [23–29]. These structures, characterized by interconnected microscale links and hinges, exhibit synchronous expansion or contraction in two directions, a property that aligns the signs of longitudinal and transverse stresses in bending, superimposing d_{31} and d_{32} modes to enhance the energy output. Li et al. [25] developed an NPR cantilever with embedded piezoelectric elements, achieving 2.76 times the output power of traditional designs. Chowdhury et al. [30] used an elliptical NPR structure to double the output power. Farhangdoust et al. [31] combined NPR and kirigami structures to enhance stretchability, further increasing the output. Gao et al. [32] introduced a layered NPR design with stronger stretchability, increasing power density by 40.73% compared to common NPR structures. Fang et al. [33] utilized these structures with centrifugal force in a rotational harvester, achieving 200.45% higher power at ultra-low rotation frequencies. Chen et al. [34] incorporated a gradient NPR structure, achieving more uniform stress distribution and 55% higher output than traditional NPR designs.

The above research adopted traditional optimization methods, which relied on trial-and-error approaches, lacking systematicity and efficiency. Recent research has demonstrated that collaborative optimization, which integrates genetic algorithms (GA) with analytical or finite element models (FEM), significantly enhances the performance of energy harvesters. Nabavi et al. [35] combined a cantilever beam voltage response analytical model (> 85% accuracy) with GA to optimize geometric parameters, achieving a 2.13-fold improvement in energy capture efficiency. Godoy et al. [36] implemented piezoelectric topology optimization via electromechanically coupled FEM, increasing energy output per unit mass. Kumar et al. [37] maximized power density through FEM-GA co-optimization of resistance, beam thickness, and proof mass length. Nabavi et al. [38] reduced resonant frequencies (first mode: 13%, second: 10%, third: 9.5%) using a COMSOL-MATLAB interface, yielding outputs of 655 mV (first mode), 80 mV (second mode), and 572 mV (third mode) under 9.8 m/s^2 excitation. However, using Finite Element Method (FEM) as a fitness function for optimization algorithms like Genetic Algorithms (GA) is computationally expensive, as it requires numerous, costly simulations. Machine learning (ML) surrogate modeling offers a solution by creating fast, approximate models that learn the relationship between design variables and performance from a limited set of data. This data-driven approach integrates design of experiments, ML, and optimization to efficiently solve complex, nonlinear engineering problems.

The above studies indicate that existing NPR energy harvesters have only considered the linear gradient variation of supercell wall thickness, while lacking efficient optimization methods. Therefore, this study proposes a novel NPR energy harvester with nonlinear gradient variations in the supercell wall thickness. This nonlinear gradient supercell wall thickness contributes to a more uniform stress–strain distribution, which further results in higher output voltage and power. In addition, ML-based optimization is utilized to simultaneously enhance the energy harvesting performance, maximizing the maximum output power and reducing the maximum stress in the piezoelectric components. On one hand, the power is improved for high-efficiency in self-powered wireless sensing; on the other hand, the maximum stress is reduced to enhance the mechanical durability of structure.

The rest of this paper is organized as follows: Section 2 outlines the structural design of the proposed energy harvester. The working principle of the harvester, along with comparative analyses against existing designs, is demonstrated using finite element simulations. Section 3 details the optimization methodology and presents the corresponding results. Experimental evaluations are provided in Section 4, covering open-circuit voltage tests, impedance matching analysis, parametric investigations, and performance validation in an IoT application scenario. Finally, Section 5 summarizes the key findings and conclusions of the study.

2. Design concept

The 3D model of the proposed negative Poisson's ratio energy harvester has re-entrant hexagonal metastructure characterized by a nonlinear gradient supercell wall thickness (NEH) as shown in Fig. 1. The system consists of a cantilever beam, a piezoelectric buzzer, and a proof mass. A cantilever beam with a re-entrant hexagonal structure is fixed to the base, with both the base and the cantilever beam made of photosensitive resin and manufactured using 3D printing methods. As shown in Fig. 1(b), a mass block is attached to the upper and lower sides of the cantilever beam free ends to reduce the resonance frequency and increase the induced vibration stress. A piezoelectric buzzer, composed of a piezoelectric sheet and brass film, is bonded to the cantilever beam using epoxy resin to generate electrical energy. When subjected to external excitation, the cantilever beam vibrates and transmits this vibration to the piezoelectric buzzer, causing its deformation. The internal piezoelectric material then converts this mechanical strain into an electric charge, generating an electrical output.

As shown in Fig. 1(c), the wall thickness increases nonlinearly from the fixed to the free end. 20 re-entrant hexagonal NPR cells are arranged on the cantilever beam and distributed in two columns and ten rows. The two columns of cells are symmetrical and identical to each other. The position near the fixed end is defined as Row 1, and the position near the free end is defined as Row 10. The structural details of the re-entrant hexagonal cell in Column 1, Row 10 are shown in Fig. 2(a) (l_1 = 8.5 mm, l_2 = 5.75 mm, l_3 = 10 mm, w = 8.4 mm, θ = 75°, t_{10} = 1.5 mm). The wall thickness (t) of the cells in each row varies nonlinearly, whereas the other parameters (l_1, l_2, l_3, w, θ) are constant. To describe the nonlinear variation in the wall thickness of the cells in each row, a cubic function is used as follows:

$$t_x = k_3 x^3 + k_2 x^2 + k_1 x + b, x = 1, 2, 3, \ldots, 10 \quad (1)$$

where x represents the row number, and t_x represents the wall thickness of row x. The cubic function is employed to describe the nonlinear

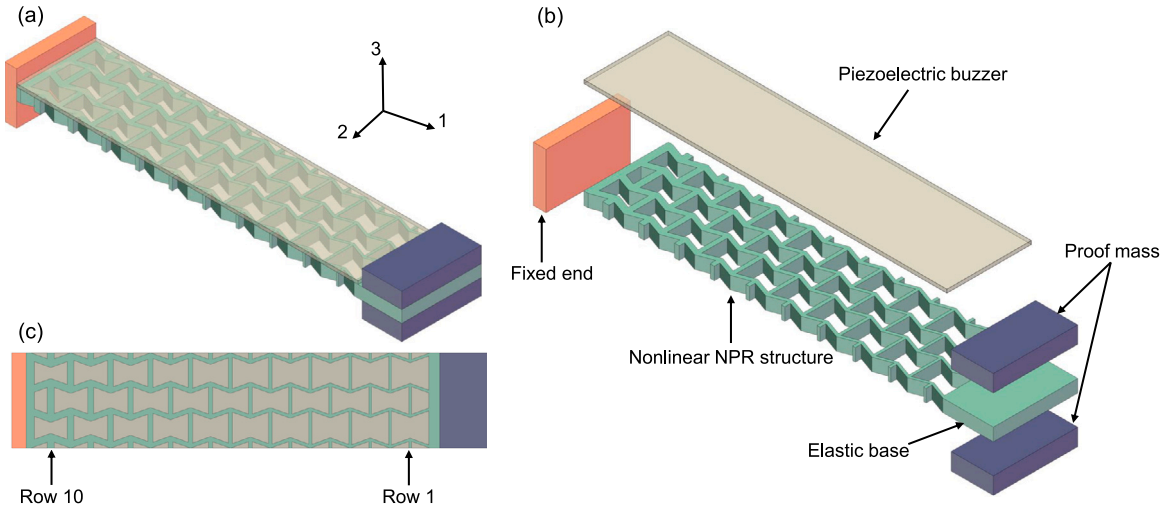

Fig. 1. The 3D model of the proposed nonlinear gradient supercell wall thickness re-entrant hexagonal energy harvester: (a) Isometric view, (b) exploded view, and (c) top view.

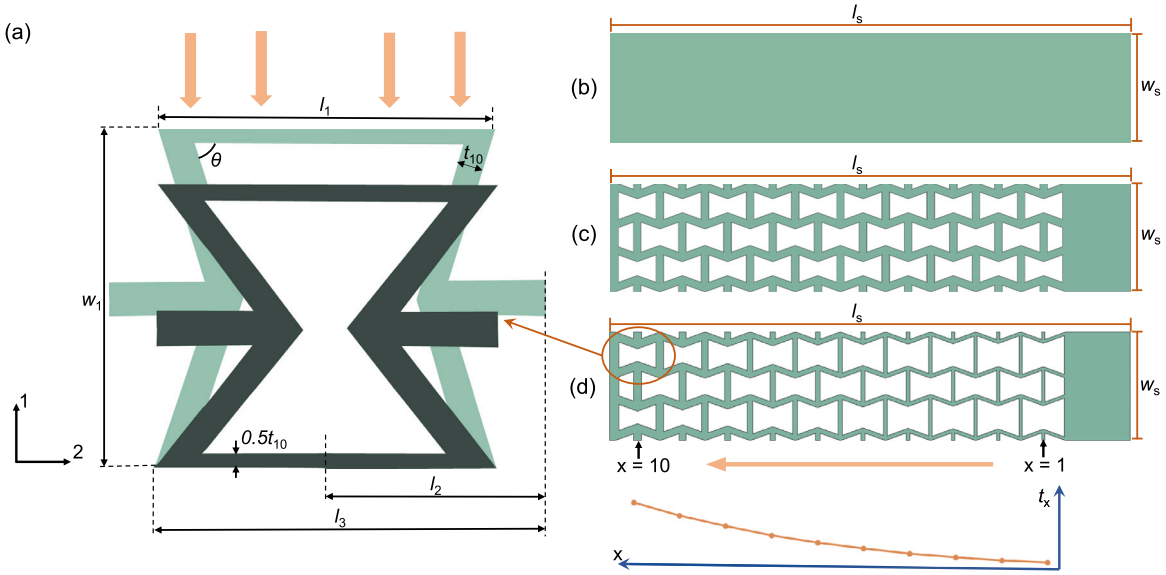

Fig. 2. (a) A re-entrant hexagonal NPR structure, (b) PEH substrate, (c) UEH substrate, and (d) NEH substrate.

variation of the wall thickness as it provides the necessary mathematical flexibility to compensate for the nonuniform stress distribution of the cantilever beam. By adjusting the coefficients k_3, k_2, k_1, and b, the structural stiffness and mass distribution can be precisely modulated to achieve a more uniform strain field across the piezoelectric patch, thereby optimizing the electromechanical conversion efficiency.

To prove the superiority of the proposed design, it is necessary to compare the proposed energy harvester with other designs. Three different energy harvester models are designed and established for comparative analysis: a traditional plain substrate (PEH), a re-entrant hexagonal substrate with a uniform wall thickness (UEH), and a re-entrant hexagonal substrate with a nonlinear gradient supercell wall thickness (NEH). As shown in Fig. 2 (b), (c), and (d), their lengths, widths, and thicknesses are identical. However, the key difference is that the latter two substrates employ different NPR structures. From Fig. 2(a), it can be observed that the unit cell contracts along 2-axis when compressed along 1-axis, as opposed to the expansion of a regular structure with a positive Poisson's ratio. This property is called the negative Poisson's ratio (NPR).

The design principles of the proposed NEH are described as follows. Based on the positive piezoelectric effect, when piezoelectric materials are subjected to mechanical stress, a charge separation phenomenon occurs on their surface, thereby forming an electric field or voltage. When a piezoelectric energy harvester operates in the bending mode, both the strain coefficients d_{31} and d_{32} ($d_{31} = d_{32}$) of the piezoelectric sheet can generate electric power. Therefore, the open-circuit voltage output of the piezoelectric sheet under this condition can be approximately expressed as:

$$U_{OC} = \frac{d_{31} t_p}{\varepsilon_{33}} \left(\overline{\sigma}_{11} + \overline{\sigma}_{22}\right) \tag{2}$$

where t_p and ε_{33} are the thickness and permittivity of the piezoelectric sheet. $\overline{\sigma}_{11}$ and $\overline{\sigma}_{22}$ are the average stresses of the piezoelectric sheet in the longitudinal (along 1-axis) and lateral (along 2-axis) directions. When the load resistance is matched to the internal impedance of the piezoelectric sheet, it can be expressed as

$$R_L = \frac{1}{2\pi f C_p} = \frac{t_p}{2\pi f \varepsilon_{33} A_p} \tag{3}$$

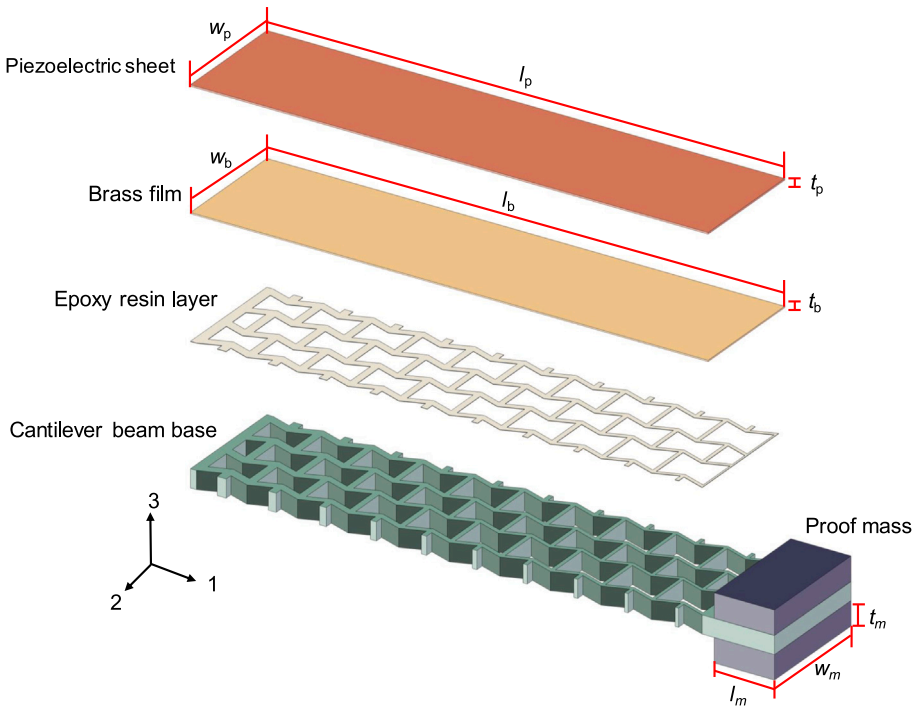

Fig. 3. Decomposition diagram of the re-entrant hexagonal energy harvester with nonlinear gradient supercell wall thickness.

where f and A_p are the excitation frequency and electrode area. Based on (1) and (2), the corresponding maximum output power generated by the piezoelectric sheet can be expressed as

$$P_{max} = \frac{\left(\frac{U_{OC}}{\sqrt{2}}\right)^2}{R_L} = \frac{\pi f t_p A_p d_{31}^2}{\varepsilon_{33}} \cdot \left(\overline{\sigma}_{11} + \overline{\sigma}_{22}\right)^2 \tag{4}$$

It can be observed from (3) that the maximum electrical power generated by the piezoelectric sheet is directly proportional to the square of the sum of the average stresses experienced (i.e., $\left(\overline{\sigma}_{11} + \overline{\sigma}_{22}\right)^2$). Therefore, compared with the traditional plain substrate ($\overline{\sigma}_{22}$ is close to zero), the substrate with the NPR structure ($\overline{\sigma}_{22}$ has the same sign as $\overline{\sigma}_{11}$) can increase the output power. In NPR structures, the thinner the wall, the greater the local stress experienced by the piezoelectric patch during vibration. Furthermore, in the cantilever beam model, the stress decreases from the fixed end to the free end during the vibration. Under the same excitation level, when the wall thickness is small, the stress is excessive, leading to the material fatigue; when the wall thickness is high, the stress is so small that the energy harvested is low. Thus, both the conditions when the wall thickness from the fixed end to the free end is uniformly small or large are not preferred from the aspects of mechanical durability or energy harvesting ability. Therefore, the NEH proposed in this work considered nonlinear gradient wall thickness for seeking the optimization design. Overall, by comparing PEH, UEH, and NEH, this strategy allows for a systematic investigation of the effects of different internal structures and wall thickness distributions on the overall performance of energy harvesters.

3. Analysis

As shown in Fig. 3, an electromechanical coupling model is built in COMSOL Multiphysics to preliminarily validate the assumed advantages of the NEH. This model consists of five main parts: a cantilever beam base, epoxy resin layer, piezoelectric sheet, brass film, and proof mass. The geometric size parameters of these components are shown in Table 1. The piezoelectric sheet and brass film are combined to form a piezoelectric buzzer. The base of the cantilever beam is manufactured from photosensitive resin using 3D printing technology and

Table 1
The geometric size parameters of the components.

Components	Parameters	Symbols	Values (mm)
Cantilever beam base	Length	l_s	97
	Width	w_s	20
	Thickness	t_s	3
Proof mass	Length	l_m	20
	Width	w_m	10
	Thickness	t_m	4
Piezoelectric sheet	Length	l_p	86
	Width	w_p	20
	Thickness	t_p	0.25
Brass film	Length	l_b	86
	Width	w_b	20
	Thickness	t_b	0.2
Epoxy resin layer	Thickness	t_e	0.05

firmly bonded to the piezoelectric buzzer with a layer of epoxy resin. The epoxy resin and cantilever beam base have the same geometric dimensions, thus ensuring the consistency and stability of the overall structure. The contact interfaces between the structural layers are modeled using a bonding constraint to enforce displacement continuity. This boundary condition ensures that the mechanical strain is fully transferred from the cantilever beam through the epoxy layer to the piezoelectric components without relative slip. The epoxy resin is defined as a linear elastic material with a thickness consistent with the experimental setup. In addition, the added proof mass helps adjust the operating frequency range of the system, making it more suitable for specific application scenarios. To ensure the convergence and accuracy of the numerical results, a mesh independence study is performed. The structure is discretized using fine tetrahedral elements, and the final mesh consists of more than 150,000 elements. This discretization level ensures that the calculated fundamental resonant frequency remains stable, with a variation of less than 1% upon further mesh refinement. This confirms that the training dataset for the surrogate model is independent of the mesh size.

Based on the finite element model, the fundamental resonant frequencies of the PEH, UEH, and NEH are identified as 44.3, 29.6,

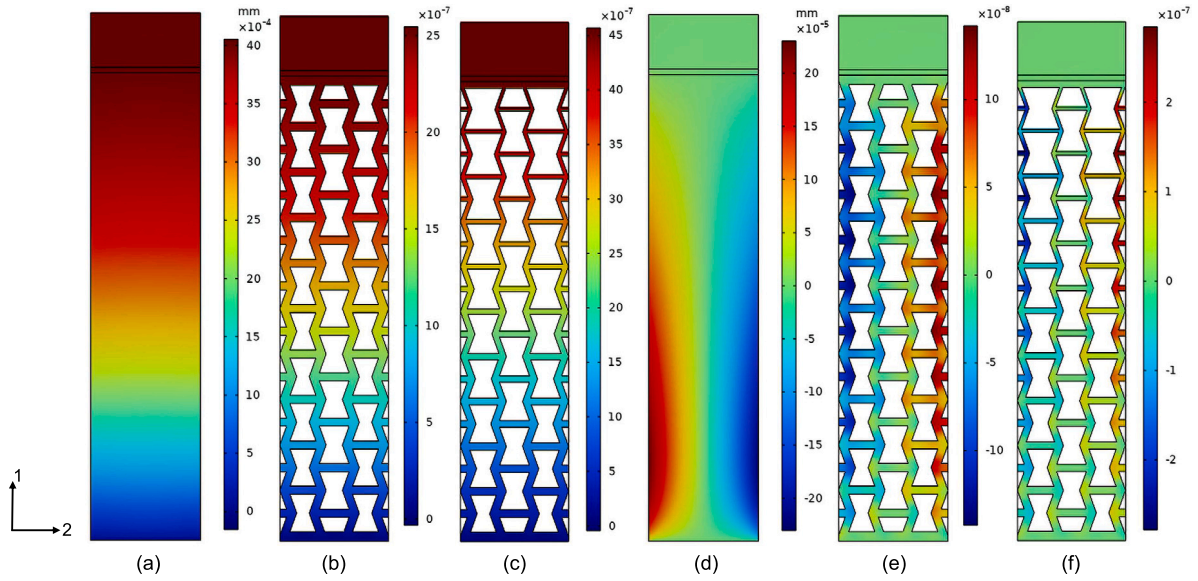

Fig. 4. Displacement distributions of the substrates: PEH along (a) 1-axis and (d) 2-axis, UEH along (b) 1-axis and (e) 2-axis, and NEH along (c) 1-axis and (f) 2-axis.

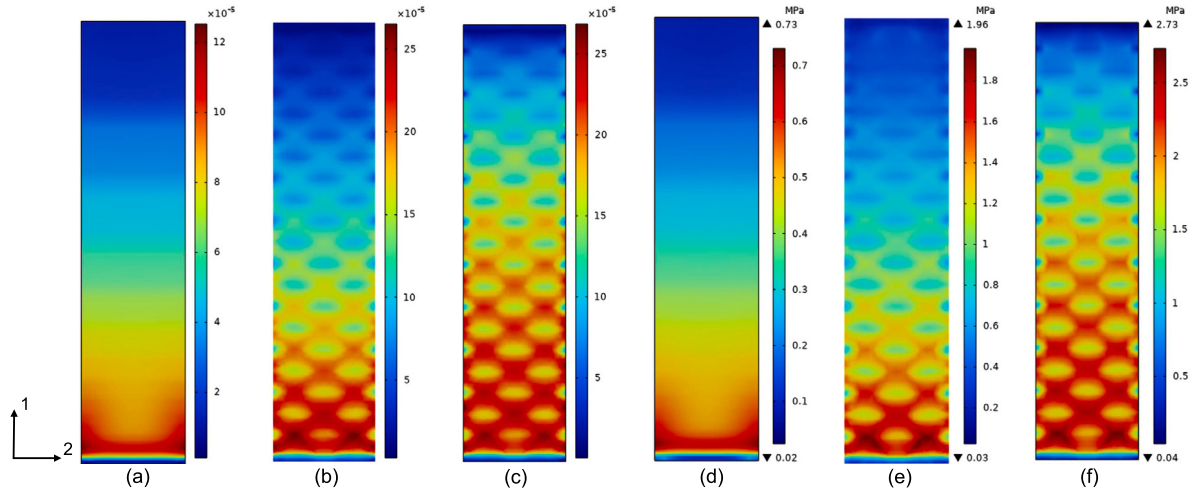

Fig. 5. Strain distributions of the piezoelectric patches in (a) PEH, (b) UEH, and (c) NEH, stress distributions of the piezoelectric patches in (d) PEH, (e) UEH, and (f) NEH.

and 24.4 Hz, respectively. The results show that introducing an NPR structure into the cantilever beam matrix can significantly reduce the resonant frequency, and introducing a nonlinear gradient supercell wall thickness design into the NPR structure can further enhance the effect of reduction. This reduction is attributed to the synergistic effect of the special mechanical behavior of the NPR structures and the wall thickness of the nonlinear gradient supercells, which jointly alter the equivalent stiffness and mass distribution characteristics of the structure.

Then, a 5 m/s^2 base excitation along 3-axis is applied to investigate the characteristics of the three energy harvesters. The longitudinal and lateral displacements of the cantilever beam base during the vibration period are shown in Fig. 4. The displacements of the three structures along the 1-axis (longitudinal) are all positive, indicating that the structures undergo tensile deformation in the longitudinal direction. Meanwhile, there are differences in the displacement conditions along the 2-axis (lateral): the lateral displacement of the PEH is negative [Fig. 4(d)], indicating that the plain substrate has contracted in the lateral direction. The lateral displacements of the UEH and NEH are both positive [Fig. 4(e) and (f)], indicating that these structures undergo tensile deformation in the lateral direction, presenting an NPR effect. Moreover, the lateral displacement of the NEH is greater than that of the UEH, indicating that the introduced nonlinear gradient supercell wall thickness design enables the re-entrant hexagonal NPR structure to have a greater displacement under the same excitation. In addition to the displacement, the strain and stress distributions of the piezoelectric patches are plotted in Fig. 5. Due to the NPR effect and the stress concentration it causes, the average strain and stress in the UEH [Fig. 5(b) and (e)] and NEH [Fig. 5(c) and (f)] are enhanced compared with those in the PEH [Fig. 5(a) and (d)]. Deduced from (1), the higher values of the average stresses with the same signs can contribute to a higher output power of the energy harvester.

Furthermore, the proposed NEH exhibits a more uniform strain and stress distribution compared to the UEH. This is because the introduction of a nonlinear gradient in supercell wall thickness further improves the uniformity of stress and strain distributions across the piezoelectric

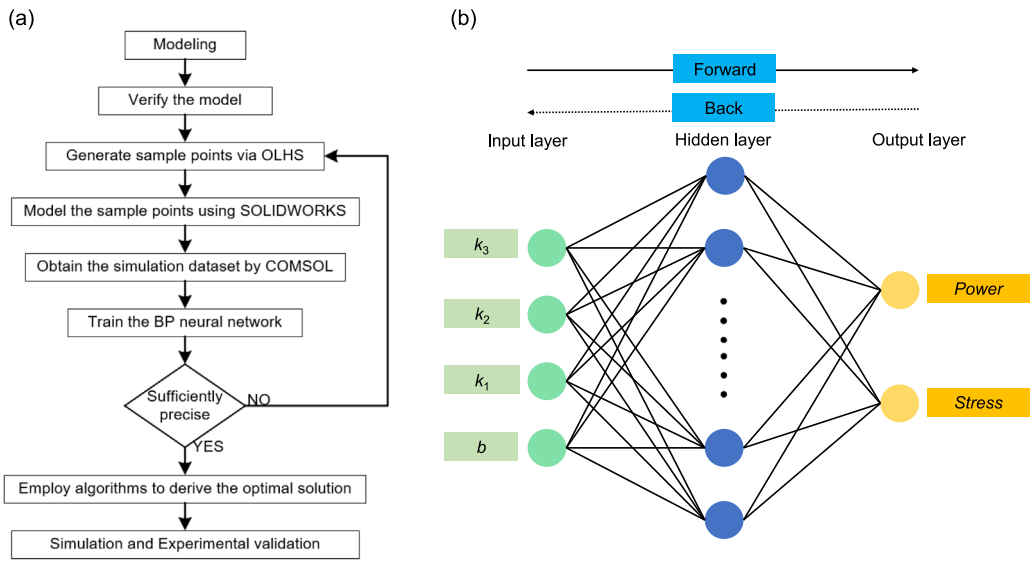

Fig. 6. The (a) flowchart of multi-objective design and (b) BP neural network model structure of the proposed energy harvester.

sheet, leading to higher average stress and strain and thus a significant enhancement in output power.

4. Optimization

Due to the complex geometric shape and multi-physics field coupling characteristics of NPR energy harvesters, traditional theoretical modeling methods are difficult to accurately establish the quantitative relationship between geometric parameters and energy harvest performance. Moreover, although NEH has a higher stress level, according to the stress-life curve, an increase in stress will lead to a decrease in fatigue lifetime. To exploit the potential of this nonlinear gradient supercell wall thickness design while achieving the best balance between the maximum output power (*Power*) and maximum stress (*Stress*) of the energy harvester, this section employs ML-based optimization techniques to conduct multi-objective optimization on the NEH. The workflow of the proposed optimization process is shown in Fig. 6(a). Firstly, the geometric parameters are initialized via optimal Latin hypercube sampling (OLHS) to generate sampling points. After modeling in SOLIDWORKS, FEA can be performed in COMSOL to obtain the *Power* and *Stress*, forming the sample dataset. Then, using this dataset, the back propagation (BP) neural network is employed to train the surrogate model and verify its accuracy. Subsequently, the non-dominated sorting genetic algorithm II (NSGA-II) method can be applied to derive the Pareto solutions. Finally, the optimal solution can be screened out from the Pareto solutions using the entropy weighted technique for order preference by similarity to ideal solution (EW-TOPSIS) method.

Specifically, an initial dataset consisting of 524 samples is obtained by using the OLHS method to generate initial samples and conducting FEA. Compared to conventional random sampling, OLHS achieves superior space filling properties by sampling each design variable exactly once at each level. This prevents the clustering of sample points and allows the surrogate model to capture the global characteristics of the design space more efficiently, which is critical for reducing the number of computationally expensive FEA simulations required for training. The inputs of the dataset are the four coefficients (k_3, k_2, k_1 and b) in the cubic function describing the nonlinear gradient supercell wall thickness of the NEH in the previous text, and the outputs are the *Power* and *Stress*. To eliminate dimensional differences and improve model performance, Z-score normalization is applied to the initial dataset, converting the original data into a standard normal distribution form with a mean of 0 and a standard deviation of 1. The standardized data not only have a unified scale but also effectively enhance the training efficiency and prediction accuracy of the model.

The architecture of the BP neural network model is shown in Fig. 6(b). The BP neural network is chosen as the surrogate model due to its robust universal approximation capabilities. Given the highly nonlinear nature of the electromechanical coupling in NPR structures, the BP network effectively bypasses the need for complex analytical derivations while providing rapid and accurate performance predictions, significantly accelerating the iterative optimization process. In this architecture, the number of neurons (n) in the hidden layer and the learning rate (α) of the optimizer will have an impact on the model performance. Therefore, the parameter analysis of n and α is required. Fig. 7 shows the parametric analysis results of the n in the hidden layer. It can be observed that when n is 10, the loss values of both the training set and the validation set are small and closest, which indicates that the model has good generalization ability. When n is 50, 250, or 1000, as the number of training iterations increases, the loss value of the training set continues to decrease, but the loss value of the validation set first decreases and then increases. This indicates that the model has experienced overfitting, that is, the model begins to over-learn the details and noise in the training data, thereby affecting its performance on unseen data. In conclusion, n is ultimately set to be 10 to achieve the best balance between the training efficiency and model performance.

Fig. 8 shows the parametric analysis results of the α. It can be observed that when α is 0.0001, although the training speed of the model is relatively slow, it can eventually converge. As α increases, the training speed of the model significantly accelerates. When α is 0.005, not only does the model have a fast convergence speed, but also the loss values of both the training set and the test set drop to an extremely low level (close to 0), indicating that the model has excellent fitting ability and generalization performance. However, when α continues to increase, the model begins to exhibit overfitting, which is manifested as a continuous decline in the loss value of the training set and a gradual increase in the loss value of the test set. In conclusion, the α is ultimately set to be 0.005 to achieve the best balance between training efficiency and model performance.

After determining the above parameters (n and α), the specific settings for the training of the model are as follows: the dataset divided into a training set (80%), a validation set (10%), and a test set (10%); the nonlinear activation function is adopted between layers to enhance the nonlinear expression ability of neural networks and overcome the limitations of linear models. During the model training process, the optimizer is used for parametric optimization ($\alpha = 0.005$), the loss

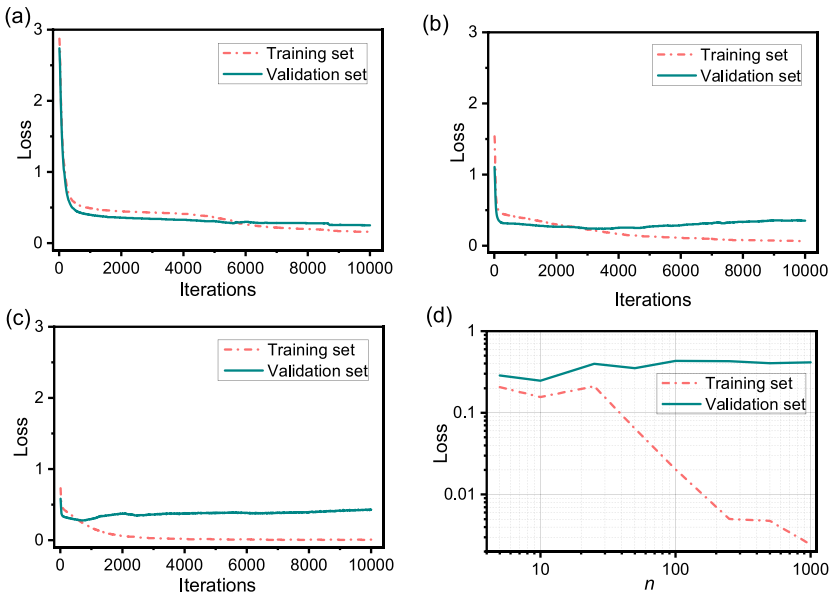

Fig. 7. The results of the number of neurons parametric analysis: (a) $n = 10$, (b) $n = 50$, (c) $n = 250$, and (d) comparison chart.

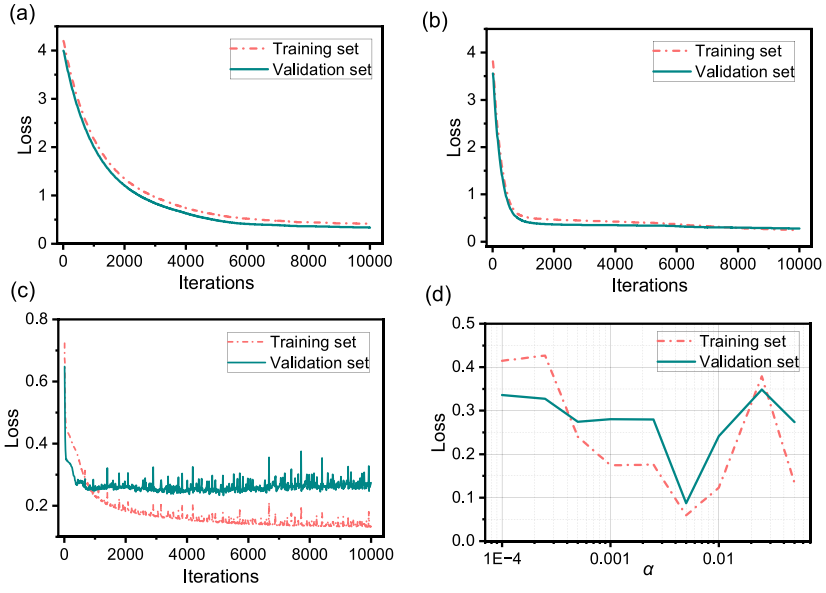

Fig. 8. The results of the learning rate parametric analysis: (a) $\alpha = 0.0001$, (b) $\alpha = 0.005$, (c) $\alpha = 0.05$, and (d) comparison chart.

function selects the root mean square error (RMSE), and the number of training iterations is set to 10000. After the model training is completed, the fitting results of the proposed energy harvester are shown in Fig. 9. The R^2 value of the *Power* in the final trained model is 0.9966, with a maximum error of 1.56% and an average error of 0.56%. The R^2 value of the *Stress* is 0.7845, with a maximum error of 8.85% and an average error of 3.46%.

Based on the ML surrogate model established above, the NSGA-II method is adopted to conduct multi-objective optimization of NEH. The advantage of employing NSGA-II lies in its elite retention strategy and its effectiveness in handling conflicting objectives, such as maximizing power while reducing stress. By utilizing a fast non-dominated sorting procedure, the algorithm maintains a diverse set of solutions, ensuring that the final Pareto front offers a comprehensive range of optimal design configurations for various application requirements.. The value range of each row wall thickness (t_x) is set to be [0.5 mm, 2 mm]. The determination of these optimization ranges is informed by the precision of the 3D printing and the need to maintain the negative Poisson's ratio effect. A minimum thickness of 0.5 mm is required to ensure structural stability during vibration, while a maximum of 2 mm prevents the structure from becoming too rigid, which would otherwise reduce the energy output at low frequencies. Therefore, the multi-objective optimization formula of the NEH can be expressed as

$$\begin{cases} \max \quad Power \\ \min \quad Stress \\ \text{s.t.} \quad \begin{aligned} &0.5 \text{ mm} \le t_x \le 2 \text{ mm}, \\ &0.45 \le b \le 1, \\ &0 \le k_1 \le 0.05, \\ &0 \le k_2 \le 0.005, \\ &0 \le k_3 \le 0.0005. \end{aligned} \end{cases} \tag{5}$$

After adjusting the algorithm parameters many times, the size of population, the number of iterations, the mutation probability, and the crossover probability are ultimately set to be 100, 200, 0.3, and 0.8,

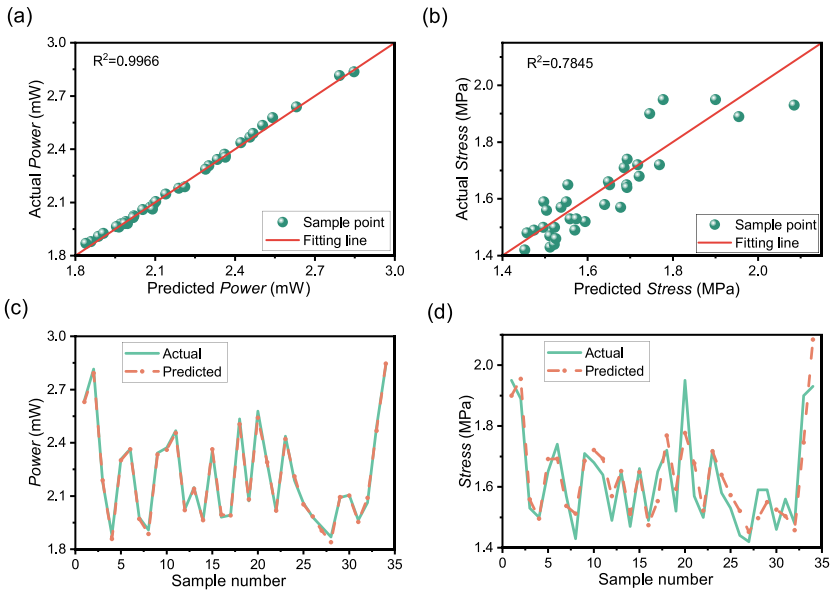

Fig. 9. The results of BP neural network fitting: the (a) *Power* scatter plot, (b) *Stress* scatter plot, (c) *Power* comparison plot, and (d) *Stress* comparison plot.

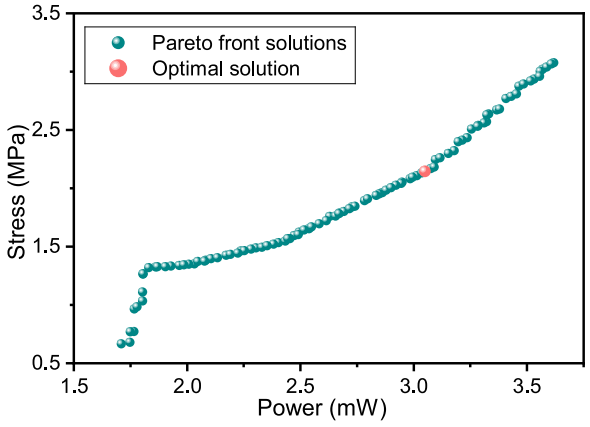

Fig. 10. The Pareto solutions of the re-entrant hexagonal energy harvester.

respectively, and binary encoding is adopted. The Pareto front solutions obtained after optimization and the optimal solution (OEH) screened out by the EW-TOPSIS method are shown in Fig. 10. It can be observed that the *Power* and *Stress* of OEH are 3.052 mW and 2.15 MPa at the optimized point, respectively. The values of the four coefficients (k_3, k_2, k_1 and b) of the OEH are ultimately set to be 5e - 4, 0, 2.348e - 3, and 0.505, respectively. To verify the accuracy of the results, FEA is conducted for verification: The maximum output power and maximum stress of OEH at 40 kΩ are 3.007 mW and 2.38 MPa, indicating the prediction error of 1.5% and 9.66% using the ML model, respectively. Specifically, results show that the *Power* and the *Stress* of the OEH have been increased by 85.41% and decreased by 11.85%, respectively, compared with those of the original NEH (1.6218 mW, 2.73 MPa).

As shown in Fig. 11(a), the output power of the re-entrant hexagonal energy harvester increases generally with rising stress. The majority of data points are concentrated on the left side of the region, exhibiting a distinct linear trend, although a small subset of data displays a scattered distribution with minor fluctuations. The operational point of the OEH falls within this linear range, indicating that the fitting model achieves a satisfactory level of accuracy in this domain. As shown in Fig. 11(b), the output power decreases with increasing frequency, demonstrating a clear negative correlation. Furthermore, the OEH maintains high output power at lower frequencies, making it well-suited for low-frequency vibrational environments. This advancement offers a novel strategy for optimizing other NPR energy harvesters.

5. Experimental validation

As shown in Fig. 12, to verify the proposed design, a vibration experimental platform is built, and its main equipment includes a computer, a vibration controller (VT-9002), a power amplifier (VSA-H132 A), a vibration table (VE-51100ST), a fan (HG-1100), an acceleration sensor, and an oscilloscope. During the experiment, the computer transmits control signals to the controller, which converts the control signals into pulse signals and transmits them to the vibration table, thereby driving the table to generate vibration. Meanwhile, the acceleration sensor will feed back the acceleration signals of the table to the controller. The controller dynamically adjusts the drive pulse signals based on the feedback signals to perform a closed-loop control.

Fig. 13(a) and (b) respectively show the back and front views of PEH, UEH, and NEH. To mitigate the discrepancies caused by manufacturing tolerances, high precision 3D printing is utilized for the cantilever substrates. The piezoelectric buzzers are bonded to the substrates by a manufacturer using an automated pattern dispensing process. This approach ensures that the epoxy resin is precisely aligned with the structural walls of the re-entrant hexagonal cells while maintaining a bonding thickness consistent with the numerical model. The patterned application is critical as it prevents resin from filling the hollow voids of the NPR structure, thereby preserving the structural flexibility required for effective strain transfer and negative Poisson's ratio effects. It can be observed in Fig. 13(b) that the substrate of PEH is plain, and the substrates of UEH and NEH contain re-entrant hexagonal structures. The supercell wall thickness of UEH is uniform, while the supercell wall thickness of NEH is nonlinear gradient. Moreover, Fig. 13(c) presents a comparison between OEH and NEH. It can be observed from Fig. 13(d) that, after optimization, the supercell wall thickness of UEH and NEH increases in each row.

An experimental inversion method is employed to identify and calibrate key simulation parameters, such as the structural damping ratio. By refining these parameters based on the measured open-circuit voltage and frequency response curves, the numerical model achieves a closer approximation of the experimental result. As evidenced by the preceding FEA, the maximum stress of OEH is lower than that of NEH. According to fatigue strength theory, the fatigue life of materials is inversely proportional to stress amplitude, suggesting that OEH is

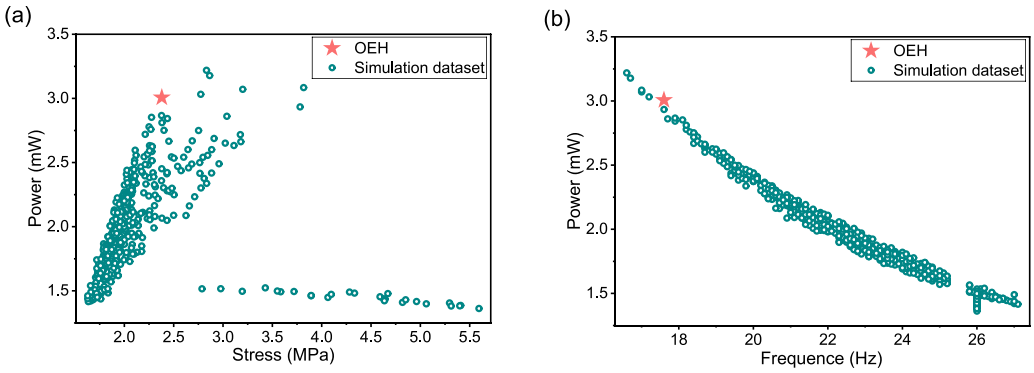

Fig. 11. The (a) stress–power diagram and (b) frequency–power diagram of the simulation dataset and OEH.

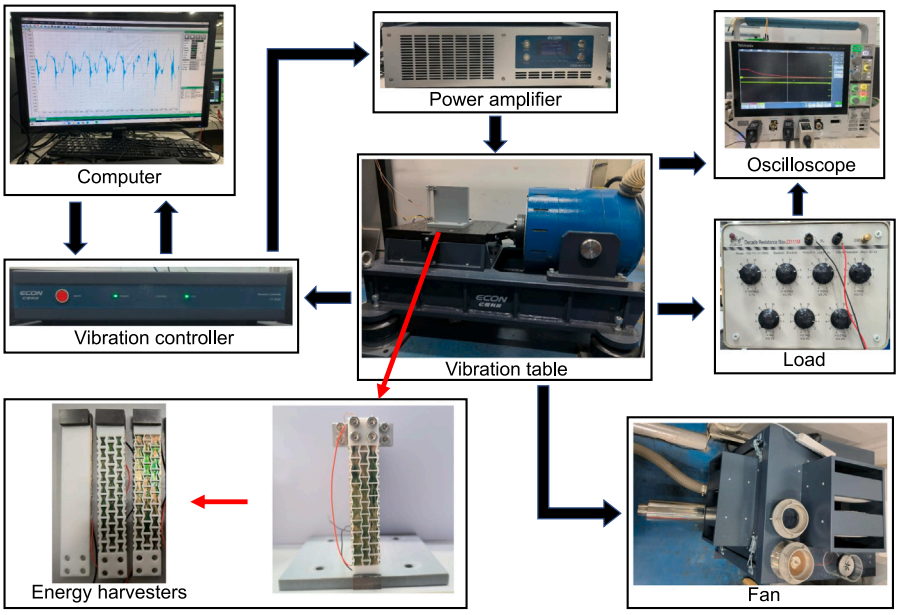

Fig. 12. The vibration experiment platform.

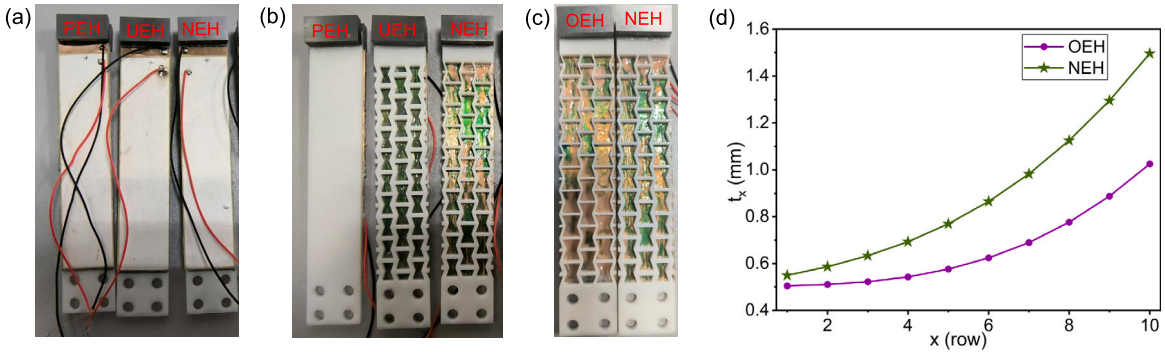

Fig. 13. The (a) back and (b) front views of the prototypes of the PEH, UEH, and NEH; the (c) front view and (d) wall thickness variations of OEH and NEH.

expected to exhibit a longer service life compared to NEH. To validate this inference, durability tests are conducted on both OEH and NEH under an excitation of 1 m/s^2 over a period of 50 h. As shown in Fig. 14, the initial open-circuit peak-to-peak voltage of NEH is 7.27 V, decreasing to 5.24 V after 50 h, representing a reduction of 27.9%. In contrast, the initial peak-to-peak voltage of OEH is 9.04 V, declining to 7.36 V after 50 h, representing a reduction of 18.58%. The voltage degradation profiles of both devices demonstrate nonlinear behavior, characterized by a relatively rapid decline within the first 10 h, followed by stabilization and fluctuation around 5.24 V (NEH) and

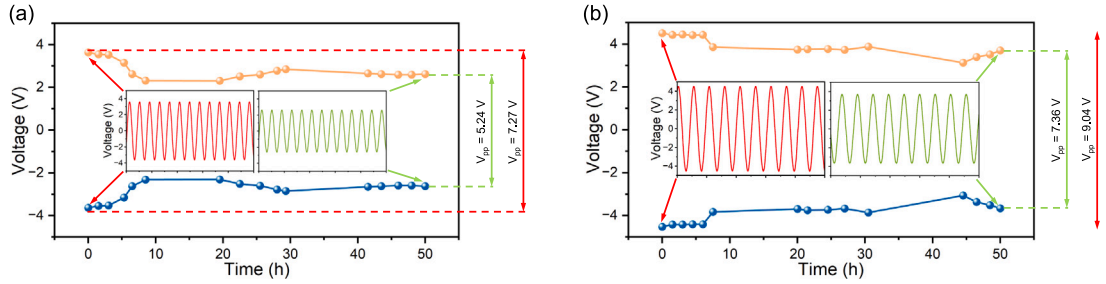

Fig. 14. The durability tests of the (a) NEH and (b) OEH.

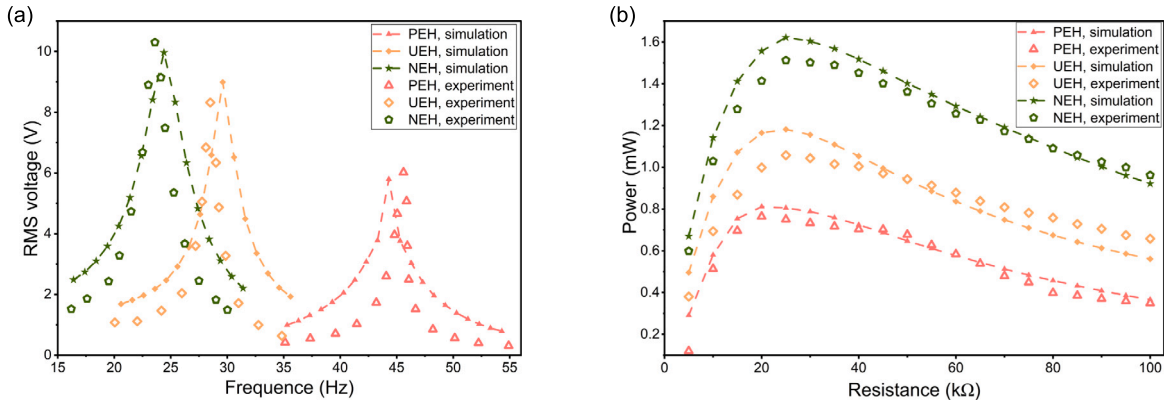

Fig. 15. The (a) open-circuit voltage output of the PEH, UEH, and NEH at different frequencies; the (b) maximum output power of the PEH, UEH, and NEH when connected to different load resistances.

7.36 V (OEH), respectively. This trend indicates that internal damage accumulation in the materials gradually reaches a state of dynamic equilibrium. The results confirm that OEH exhibits superior retention of electrical performance during prolonged operation, demonstrating enhanced durability and supporting the earlier life expectancy prediction based on stress levels.

As shown in Fig. 15(a), to verify the superiority of the proposed NEH, the frequency response test at 5 m/s^2 under open-circuit condition is first conducted to identify the resonant frequencies of the PEH, UEH, and NEH, which are found to be 45.6, 28.5, and 23.6 Hz, respectively. The simulation errors of their resonant frequencies are 2.93%, 3.72%, and 3.28%, respectively, which are relatively small. This verification process confirms the accuracy of the FEA simulation model. After that, they are connected to load resistance for measuring output power, and the impedance matching results are plotted in Fig. 15(b), where the maximum output power of PEH, UEH, and NEH reaches 0.764, 1.0573, and 1.5121 mW at 20, 25, and 25 kΩ, respectively.

Furthermore, the corresponding power mass densities of these energy harvesters are found to be 27.84, 43.55, and 64.34 μW/g, respectively. Therefore, it can be found that compared with UEH and PEH, the power mass and volume density of NEH are increased by 47.6% and 131.1%, 43% and 97.9%, respectively, proving the effectiveness of the introduced nonlinear gradient supercell wall thickness design in NEH.

As an upgrade of NEH, the resonance frequency of the OEH is found to be 17.6 Hz and the maximum output power at 40 kΩ is 2.831 mW. Fig. 16 presents the maximum output power of OEH and NEH when connected to different load resistances, validating the effectiveness of the optimization method. In addition, the power mass density of OEH reaches 124.89 μW/g, which increases 94.1%, 186.8%, and 348.56% compared with that of NEH, UEH, and PEH, respectively.

Moreover, the normalized power density (NPD) of OEH is compared with that of the existing NPR piezoelectric energy harvesters obtained from references, further proving the superiority of the proposed design.

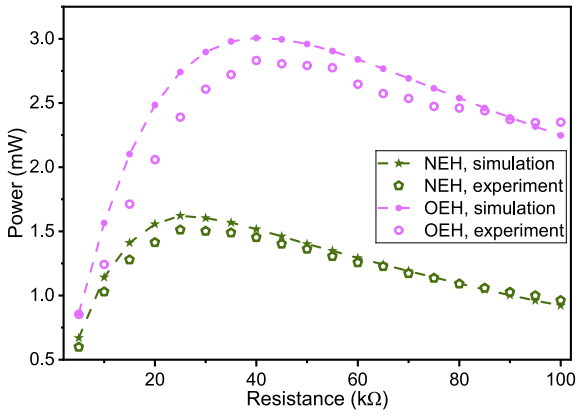

Fig. 16. The maximum output power of the OEH and NEH when connected to different load resistances.

The NPD (max power divided by the volume of the piezoelectric sheet and the resonant frequency) of the energy harvesters is summarized in Table 2. The NPD of OEH is 374.11 μW cm^{-3} Hz^{-1}, which is higher than those of existing energy harvesters. This indicates that the proposed energy harvester has superior energy harvesting performance at low frequencies.

After that, to validate the proposed energy harvester to stably supply power for Internet of Things (IoT) devices under low-frequency vibration conditions, the previous vibration experimental platform is combined with wireless IoT devices to construct the vibration-powered sensing system (VPSS). The utilized IoT device is depicted in Fig. 17(a), where the red board is the rectifier bridge, the blue board is the energy storage module (ESM), the black board is the energy user module (EUM), and the green board is the long-range (LoRa) module. When the system is subjected to vibration excitation, the energy harvester

Table 2
The performances of NPR piezoelectric energy harvesters in the literature.

References	$Volume_{Piezo}$ (cm^3)	Resonant frequency (Hz)	Max power (μW)	NPD (μW cm^{-3} Hz^{-1})
Eghbali et al. [26]	0.072	181.91	2030	154.99
Li et al. [25]	1	–	690	–
Eghbali et al. [29]	–	59	60.1	–
Ferguson et al. [39]	0.072	10	191.1	265.42
Chen et al. [24]	0.12	7.19	122.65	142.15
Kabirian et al. [40]	0.16	106	3150	185.73
Gao et al. [32]	0.36	–	5660	–
This work	0.43	17.6	2831	374.11

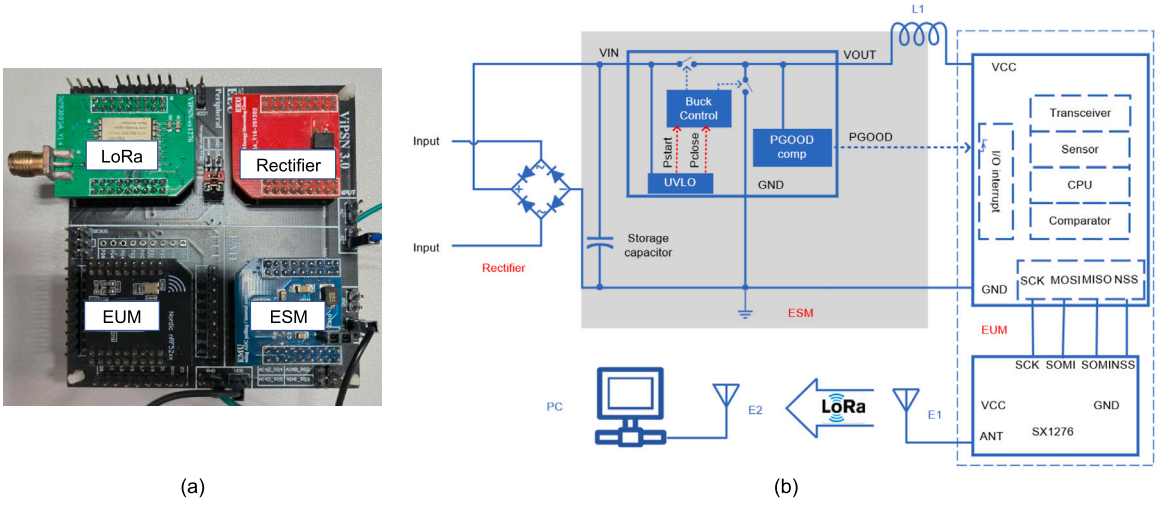

Fig. 17. Schematic of the (a) IoT device and the (b) corresponding circuit topology diagram.

converts the environmental vibration energy into alternating current through the piezoelectric effect. As shown in Fig. 17(b), the alternating current is first converted into direct current by the rectifier bridge, which is stored in the capacitor in the ESM. Then, the ESM adjusts the voltage to an appropriate level to supply power to the EUM and LoRa module. EUM performs temperature perception and data transmission tasks. The LoRa module transmits the data collected by the EUM over a long distance to the computer via wireless communication.

Besides, under an excitation of 5 m/s^2, the corresponding vibration frequencies for NEH and OEH are 23.6 Hz and 17.6 Hz, respectively. As shown in Fig. 18(a), the vibration drive system, energy harvesters, and sensing end are deployed in the indoor laboratory, and the receiving end is placed approximately 200 m outdoors. As shown in Fig. 18(c) and (d), the oscilloscope records the variations of each key voltage signal during the system operation. The energy accumulation and signal transmission stages of NEH and OEH last approximately 120 s and 75 s, respectively, indicating that the energy accumulation and signal transmission efficiency of OEH is 37.5% higher than that of NEH. It has been verified that due to the high output power of OEH, it can achieve real-time self-powered temperature transmission at short time intervals. As shown in Fig. 18(b), the computer successfully receives four signals, corresponding to the four-voltage jump-drops of the OEH recorded by the oscilloscope, indicating that the signal transmission is stable and reliable. Overall, the experimental results verify the feasibility and stability of the proposed NEH and OEH in vibration-driven self-powered wireless sensing systems.

6. Conclusion

Although vibration energy harvesters have been widely utilized to provide sustainable power for IoT devices, miniaturized cantilever piezoelectric energy harvesters often exhibit insufficient power at low frequencies. In this article, an NEH is proposed to improve the efficiency of vibration piezoelectric energy harvesting by introducing a nonlinear gradient supercell wall thickness design into the NPR structure. Compared with the traditional UEH, the NEH has a lower resonant frequency, greater displacement, and more uniform stress and strain distribution, which can contribute to a higher output power. In addition, ML-based optimization techniques are also utilized to conduct multi-objective optimization for the NEH. FEA is performed to explore the performance of the energy harvesters, which shows that the maximum stress of the OEH is reduced by 11.85% compared with that of UEH. This simulation result verifies that the proposed design is beneficial for the lifetime of the energy harvester.

In the experimental validation, under the excitation of 5 m/s^2, the power density of NEH reaches 64.34 μW/g, increased by 47.6% and 131.1% compared with UEH and PEH, respectively. This proves that the introduced nonlinear gradient supercell wall thickness design in NEH can effectively improve the efficiency of the energy harvesting. Besides, through optimization, the power density of OEH reaches 124.89 μW/g, which is further increased by 94.1% compared with the original NEH. This validates the effectiveness of the optimization method and demonstrates the potential of the nonlinear gradient supercell wall thickness design. Furthermore, in IoT application testing, under the excitations of 5 m/s^2, NEH and OEH respectively support the IoT system to transmit temperature signals once every 120 s and 75 s, verifying their good stability. Moreover, the transmission efficiency of OEH is 37.5% higher than that of NEH, demonstrating the ability of the proposed OEH to exhibit sufficient power for IoT devices at a lower frequency.

In future work, attempts can be made to introduce the nonlinear gradient supercell wall thickness design into other types of NPR energy harvesters beyond the re-entrant hexagon, thereby further expanding their applicability and potential for performance improvement across different structures. In application, the proposed harvester offers advantages for diverse sensing networks in smart cities, aerospace, and marine engineering. It facilitates autonomous operation for structural health monitoring of urban infrastructure, wireless strain sensing for

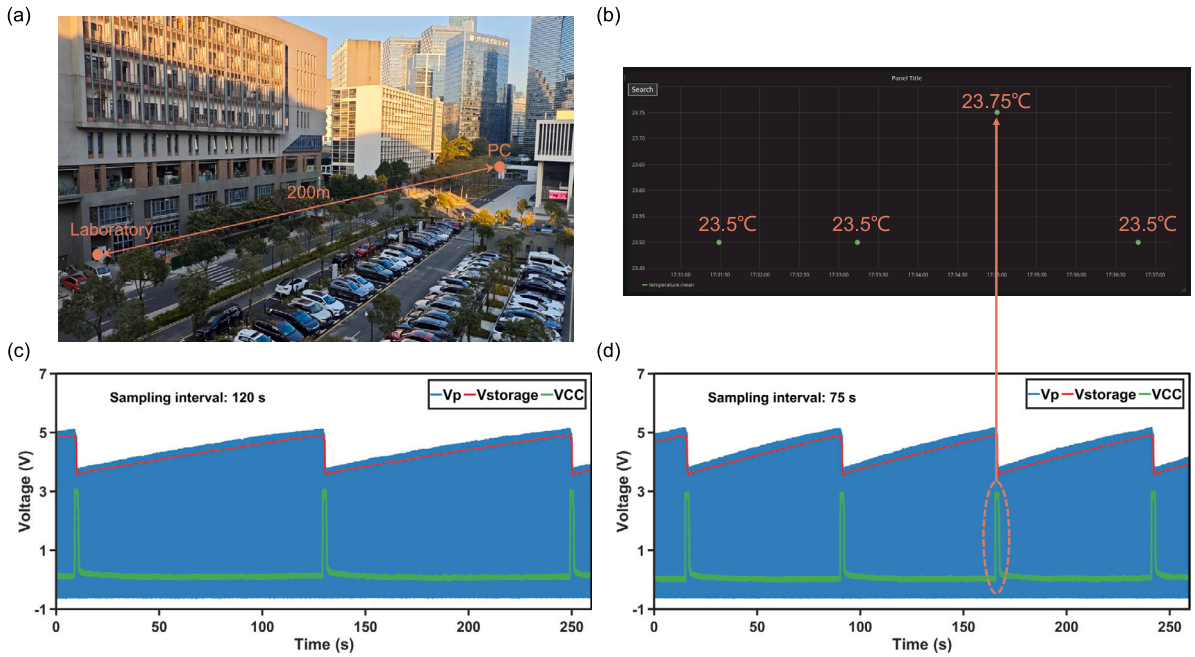

Fig. 18. The (a) sensing distance test scenario; the system voltage timing curve using (b) OEH and (c) NEH; the (d) computer successfully receives temperature data.

aircraft airframes, and environmental monitoring in marine information networks. These applications address the challenge of battery replacement in areas where manual intervention is impractical. Additionally, although this study successfully verifies the performance of NEH and OEH in vibration-driven wireless sensing systems under laboratory conditions, no protective measures are implemented for the energy harvesters. Subsequent studies will focus on developing specialized packaging and protective measures to ensure the stability and reliability of the device in complex and harsh environments.

CRediT authorship contribution statement

Shitong Fang: Writing – original draft, Validation, Project administration, Methodology, Investigation, Funding acquisition, Conceptualization. **Jinkang Liu:** Writing – original draft, Visualization, Validation, Investigation. **Yufeng Guo:** Software, Methodology, Investigation, Data curation. **Qingyang Xu:** Visualization, Software, Resources. **Kui Wu:** Visualization, Investigation. **Yi Guan:** Visualization, Investigation. **Liuchao Jin:** Writing – review & editing, Validation. **Zhihui Lai:** Writing – review & editing, Project administration. **Mingjing Cai:** Writing – review & editing, Resources, Project administration. **Keyu Chen:** Writing – review & editing, Investigation. **Wei-Hsin Liao:** Writing – review & editing, Supervision, Project administration, Investigation, Funding acquisition.

Funding

This work was funded by National Natural Science Foundation of China (Grant No. 52575130), Guangdong Basic and Applied Basic Research Foundation (Grant No. 2026A1515010148), Shenzhen Natural Science Fund (Grant No. JCYJ20230808105206013), Hong Kong Research Grants Council (Grant Nos. CUHK 14211823 and STG5/E-103/24-R), Hong Kong Innovation and Technology Commission (Project No. ITS/348/24), and The Chinese University of Hong Kong (Grant No. 4935121).

Declaration of competing interest

The authors declare that they have no known competing financial interests or personal relationships that could have appeared to influence the work reported in this paper.

Data availability

Data will be made available on request.

References

[1] Jing H, Xiang H, Wang J. Theoretical modeling of wall-proximity effect for vortex-induced vibration energy harvesting in tunnel. Energy 2025;139723.
[2] Guan Yi, Li Xin, Wei Zehan, Xiao Mianxin, Lai Zhihui, Dong Shuxiang, Yurchenko Daniil, Fang Shitong. Bistable multi-layer triboelectric nanogenerator for harvesting random and ultra-low-frequency vibration energy with increased charge transfer. Adv Sci 2025;e05246.
[3] Zhao Lin-Chuan, Chen Ze-Wen, Gao Qiu-Hua, Wu Zhi-Yuan, Yan Ge, Wei Ke-Xiang, Meng Guang, Zhang Wen-Ming, Zou Hong-Xiang. Self-aligning mechanism for wearable biomechanical energy harvesters. Device 2026;4(1):100972.
[4] Zhang Bin, Yang Guang, Hu Bingxin, Xiong Yeping, Zhou Shengxi. Optimized design of self-powered SSHI interface circuit for enhanced vibration energy harvesting. Smart Mater Struct 2025;34(2):025025.
[5] Xing J, Zhu F, Yu M. Omnidirectional piezoelectric energy harvesting with triple-V-beam spherical joint structure for hybrid vibration and wind energy conversion. Energy 2025;341:139382.
[6] Nie Qiyi, Wang Fei, Yang Feng-Shou, Xun Hanzhi, Hou Jiachen, Xu Qingyang, Hong Ying, Zhang Jingyu, Wei Xueyong, Lin Yen-Fu, Chiu Po-Wen, Zeng Longhui, Li Mengjiao, Wang Biao, Zhang Jianhua. Tactile perception revolution: Innovations in flexible FET-based tactile sensors for next-genhuman–machine interfaces. Adv Mater 2026. 0:e10646.
[7] Tan D, Ou X, Jia Z, et al. A cylindrical bistable hybrid triboelectric-electromagnetic energy harvester for harvesting low-frequency vibration energy. Energy 2025;137597.
[8] Fang Shitong, Zhang Xiao, Fan Junwei, Guan Yi, Liu Wenlong, Cai Mingjing, Lai Zhihui, Huang Xingbao, Wang Xiaosun, Zhou Shengxi, et al. A high-output dynamic bistable electromagnetic energy harvester for ultra-low-frequency rotational excitations. Mech Syst Signal Process 2026;246:113925.
[9] Cai Mingjing, Liao Wei-Hsin. Toward high-performance wrist-worn energy harvester via hybrid approach. IEEE/ASME Trans Mechatronics 2025;30(1):469–81.
[10] Zhao Y, Cui H. Vibration suppressing and energy harvesting research of an elastic beam by utilizing an adjustable imperfect nonlinear energy sink. Energy 2025;322:135663.
[11] Yan Bo, Ling Peng, Miao Lunlun, Yu Ning, Sun Jiaojiao, Li Qinchuan. Ultra-low frequency vibration isolation of cockroach-inspired structures with electromagnetic shunt damping enhanced by geometric nonlinearity. IEEE/ASME Trans Mechatronics 2023;29(1):476–86.
[12] Fang Shitong, Wang Xiying, Zhang Xiao, Wu Kui, Yan Tao, Chuai Xinyuan, Huang Xingbao, Li Xin, Lai Zhihui, Dong Shuxiang, et al. High output, lightweight and small-scale rotational piezoelectric energy harvester utilizing internal impact effect. Energy Convers Manage 2024;322:119180.

[13] Zhong L, Liu R, Sun Y, et al. A flexible piezoelectric film for fluid energy harvesting using wake-induced vibration. Energy 2025;139344.
[14] Tian Haigang, Fan Wenshuai, Zhang Wenming, Tang Lihua, Wang Junlei. Enhanced performance of piezoelectric energy harvester incorporating surface protrusions. Energy 2025;139613.
[15] Ma Xiaoqing, Li Haitao, Zhou Shengxi, Yang Zhichun, Litak Grzegorz. Characterizing nonlinear characteristics of asymmetric tristable energy harvesters. Mech Syst Signal Process 2022;168:108612.
[16] Ma Xiaoqing, Ma He, Zhou Shengxi. Nonlinear analysis and response identification of tristable energy harvesters under wind and base excitations. Int J Non-Linear Mech 2025;173:105052.
[17] Nabavi S, Zhang L. T-shaped piezoelectric structure for high-performance MEMS vibration energy harvesting. J Microelectromech Syst 2019;28(6):1100–12.
[18] Yang Z, Wang YQ, Zuo L, et al. Introducing arc-shaped piezoelectric elements into energy harvesters. Energy Convers Manage 2017;148:260–6.
[19] Ibrahim D Sh, Beibei S, Fatai S, et al. Numerical and experimental study of a gauge-shaped beam for improved performance of piezoelectric energy harvester. Microsyst Technol 2021;27(12):4253–68.
[20] Malakooti MH, Sodano HA. Piezoelectric energy harvesting through shear mode operation. Smart Mater Struct 2015;24(5):055005.
[21] Xu C, Ren B, Di W, et al. Cantilever driving low frequency piezoelectric energy harvester using single crystal material 0.71Pb(Mg1/3Nb2/3)O3-0.29PbTiO3. Appl Phys Lett 2012;101(3):033502.
[22] Yang Z, Zu J. High-efficiency compressive-mode energy harvester enhanced by a multi-stage force amplification mechanism. Energy Convers Manage 2014;88:829–33.
[23] Chen K, Fang S, Lai Z, et al. A plucking rotational energy harvester with tapered thickness and auxetic structures for increasing power output. Appl Energy 2024;357:122490.
[24] Chen K, Fang S, Gao Q, et al. An auxetic nonlinear piezoelectric energy harvester for enhancing efficiency and bandwidth. Appl Energy 2021;298:117274.
[25] Li Q, Kuang Y, Zhu M. Auxetic piezoelectric energy harvesters for increased electric power output. AIP Adv 2017;7(1):015104.
[26] Eghbali P, Younesian D, Farhangdoust S. Enhancement of piezoelectric vibration energy harvesting with auxetic boosters. Int J Energy Res 2020;44(2):1179–90.
[27] Chen K, Fang S, Gao Q, et al. An enhanced nonlinear piezoelectric energy harvester with multiple rotating square unit cells. Mech Syst Signal Process 2022;173:109065.
[28] De Bellis ML, Bacigalupo A. Auxetic behavior and acoustic properties of microstructured piezoelectric strain sensors. Smart Mater Struct 2017;26(8):085037.
[29] Eghbali P, Younesian D, Moayedizadeh A, et al. Study in circular auxetic structures for efficiency enhancement in piezoelectric vibration energy harvesting. Sci Rep 2020;10(1):16338.
[30] Roy Chowdhury A, Saurabh N, Kiran R, et al. Effect of porous auxetic structures on low-frequency piezoelectric energy harvesting systems: a finite element study. Appl Phys A 2022;128(1):62.
[31] Farhangdoust S, Georgeson G, Ihn JB, et al. Kirigami auxetic structure for high efficiency power harvesting in self-powered and wireless structural health monitoring systems. Smart Mater Struct 2021;30(1):015037.
[32] Gao Q, Lu Y, Shi Y, et al. Enhancing the output performance of energy harvesters using hierarchical auxetic structure and optimization techniques. IEEE Trans Ind Electron 2024;71(9):11641–9.
[33] Fang S, Chen K, Lai Z, et al. Analysis and experiment of auxetic centrifugal softening impact energy harvesting from ultra-low-frequency rotational excitations. Appl Energy 2023;331:120355.
[34] Chen K, Fang S, Gao Q, et al. Enhancing power output of piezoelectric energy harvesting by gradient auxetic structures. Appl Phys Lett 2022;120(10):103901.
[35] Nabavi S, Zhang L. MEMS piezoelectric energy harvester design and optimization based on Genetic Algorithm. In: IEEE international ultrasonics symposium. Tours, France: IEEE; 2016, p. 1–4.
[36] Godoy TCD, Trindade MA, Deü JF. Topological optimization of piezoelectric energy harvesting devices for improved electromechanical efficiency and frequency range. In: Blucher mechanical engineering proceedings. Blucher; 2014, p. 4003–16.
[37] Kumar A, Sharma A, Kumar R, et al. Finite element analysis of vibration energy harvesting using lead-free piezoelectric materials: A comparative study. J Asian Ceram Soc 2014;2(2):139–43.
[38] Nabavi S, Zhang L. Design and optimization of wideband multimode piezoelectric MEMS vibration energy harvesters. In: Proceedings of eurosensors 2017. Paris, France: Eurosensors; 2017, p. 586.
[39] Ferguson WJG, Kuang Y, Evans KE, et al. Auxetic structure for increased power output of strain vibration energy harvester. Sensors Actuators A: Phys 2018;282:90–6.
[40] Kabirian Z, Ebrahimian F, Younesian D, et al. Inlay-inspired meta-piezoelectric plates for the low-frequency vibration energy harvesting. J Mater Sci, Mater Electron 2022;33(6):2909–20.